

# Cobalt ferrite $\text{CoFe}_2\text{O}_4$ films' preparation, description, and their application restrictions in an alcoholic medium

Mostafa. R. Hussein\*<sup>1</sup>, Elsayed. M. Elsayed<sup>2</sup>, Ibrahim. A. Ibrahim<sup>2</sup>

<sup>1</sup>Nanotechnology and Material Science Department, Faculty of Postgraduate Studies for Advanced Science (PSAS), Beni-Suef university, Beni-Suef, Egypt.

<sup>2</sup>Central Metallurgical Research and Development Institute (CMRDI), Helwan, P.O. Box 87, Cairo 11421, Egypt.

\*Corresponding author: E-mail: [Moustafa.rashad@psas.bsu.edu.eg](mailto:Moustafa.rashad@psas.bsu.edu.eg)

Received 24 November 2022

Accepted 22 June 2023

Published 31 December 2023

## Abstract

On various substrates,  $\text{CoFe}_2\text{O}_4$  thin films were produced via an electrodeposition-anodization technique using a non-aqueous sulphate solution. At room temperature, the deposited alloy was electrochemically anodized (1M KOH) into the appropriate hydroxide. The cyclic voltametric procedure was performed to examine the electrodeposition of Co-Fe alloy on different substrate materials, to optimize the oxidation and reduction processes occurring on separate electrodes' surfaces. The Galvanostatic technique was used to adjust the formation of the initial deposits. Also, the technique of polarisation through potentiodynamics was accustomed to evaluate the ferrite's resistance to corrosion on each substrate material and its stability. X-ray diffraction, SEM, and vibrating sample magnetometer techniques were done to examine crystalline construction, crystallite dimension, morphology, and the magnetic behaviours of ferrite layers. The data collected showed that cobalt ferrite nanoparticles deposited on Pt, SS, and Cu substrates enhanced the magnetic and electrochemical properties. The corrosion rate results demonstrated  $\text{CoFe}_2\text{O}_4$  thin film for Pt and SS substrates may be employed safely in highly acidic and alkaline environments (high corrosion resistance), with the exception of pH = 9, Cu substrates are inert at all pH values.

**Keyword:** Ferrites; Nanoparticles; Cyclic voltammetry; Corrosion rate; Polarization Curves

## 1. Introduction

Spinel ferrite components have attracted attention recently due to its potential technological applications,  $\text{MFe}_2\text{O}_4$  nanoparticles (M denotes metal with two valences ion e.g., Cu, Mg, Mn, Ni, Fe, etc.) such as in multilayer chip inductors, EMI overpowering, gas detection, transformer cores, antenna rods, inductors, magnetic loudspeakers, radio frequency paths, high-quality filters, power transformers in microelectronics, and read/write heads for high-speed digital tape [1-11]. High magnetic properties distortion, which is created in the spin-orbit (L-S) coupled with crystal frames, is the principal reason for the use of Co-ferrite for medical applications. The special physical and mechanical properties of cobalt ferrite ( $\text{CoFe}_2\text{O}_4$ ) lead to its wide-

ranging application in nanomedicine. It is a rigid, high-curie magnetic matter [12]. It also has good chemical reactivity, mechanical stability, resistance to wear, and electric protection.

Because of the high-power density that has been collected in the solution close to the cathode surface, electrodeposition is a potent and intriguing technique that can be used to create layers and powders [13]. For large-scale applications, electrochemical oxide layer production is cost-effective and acceptable [14-15]. There are no by-product species since electricity performs oxidation and reduction [14]. The method uses a low processing temperature and requires little in the way of raw ingredients or equipment. It uses

electrochemical factors to regulate the composition and form of the film. This refers to its ability to build-up a film on a cathode surface. Making large-area electrodes without vacuum is easiest [13]. Nanocrystalline films that are homogeneous, fine, and reproducible are produced [16-18].

Despite the simple fact that metallic layers have frequently been obtained via electrochemical deposition from aquatic media. In some circumstances, using non-watery arrangements offers a variety of interesting benefits. To begin, an aqueous shell is put to the nanoparticle's surface after it has been created via electrodeposition in a non-aqueous fluid.

As a result, diffusing the nanoparticle in aqueous solutions is simple. This is a basic characteristic required for most biological applications [19-21]. Due to the physical and chemical characteristics of transition metals, nano ferrites are extremely sensitive to the method of preparation. Ferrite MNPs' physical characteristics, such as size, shape, and magnetism, can be dramatically altered by the synthesis circumstances as well as synthetic materials. The current study describes the electrochemical deposition process used to create  $\text{CoFe}_2\text{O}_4$  thin layers from alcoholic sulphate bath on various cathodes., because the crystallographic texture of the substrates significantly affects the properties of nanocrystalline deposited films. The current work's objective was to concentrate on the investigation of the influence of varying the cathode type and annealing temperature on the electrodeposition of cobalt ferrite from a non - aqueous sulphate bath by using electrochemical techniques: cyclic voltammetry and galvanostatic measurements.

Also, to study the electrochemical behaviour, at different pH values (1.0, 3.0, 7.0, 9.0, and 12.0), of the prepared nanocrystalline cobalt ferrite  $\text{CoFe}_2\text{O}_4$  thin films.

## 2. Material synthesis

In this paper. Thin cobalt ferrite layers were formed on various surfaces utilizing an electrochemical process. The effects of production parameters such as current density, bath composition, substrates, film thickness, time, pH, and annealing temperature were studied. Analytical grades of ammonium ferrous sulphate hexa- hydrate ( $\text{Fe}(\text{NH}_4)_2(\text{SO}_4)_2 \cdot 6\text{H}_2\text{O}$ ) and cobalt sulphate hepta-hydrate ( $\text{CoSO}_4 \cdot 7\text{H}_2\text{O}$ ), were employed to deposit the related metal alloys. Ethyl alcohol was utilised as an alcoholic medium. for deposition from non-aqueous medium electrolyte which was kept unstirred. Electrodeposition processes were performed using freshly prepared solutions. The

solution's acidity was maintained at 3. by utilising 0.5 M  $\text{H}_3\text{BO}_3$ . In addition to its role in achieving the preferred orientation of the  $\text{CoFe}_2$  alloy deposition, as a brightener, 0.2 M saccharin was utilized [22].

The metallic alloys were anodized with the appropriate hydroxide using a 1 M potassium hydroxide solution. As surfaces, thin sheets (thickness 2-3 mm) of platinum (Pt), stainless steel (SS), and copper (Cu) were utilised, with the backsides coated with isolating tape. The cathode area ranged from 1 to 2.5  $\text{cm}^2$ . The metal substrates were detergent-cleaned, ultrasonically cleaned in double-distilled water, treated with acetone, methanol, and drying [23].

Each substrate was anodically etched for 5 minutes prior to deposition at a fixed anodic applied current of 10  $\text{mA}/\text{cm}^2$ .



**Fig. 1** Experimental set-up of electrochemical method.

Figure 1 depicts a schematic representation of the experimental apparatus utilised for alloy deposition. It is composed mostly of a Pyrex frame, a bath container, an auxiliary electrode (anode), and a substrate (cathode). In comparison to the standard hydrogen electrode, a silver/silver chloride reference electrode saturated in KCl ( $E_o = 0.200 \text{ mV}$ ) was utilised (SHE).

A computer-controlled Potentiostat (Volta Lab 21) PGP201 Potentiostat, Galvanostat 20 V, 1A with typical power supply was used to complete electrochemical polarisation investigations (Tafel Plot) and electrodeposition tests. The entire potential scan for anodic and cathodic potentiodynamic polarisation (Tafel plots) was timed to occur within 250 mV of the corrosion potential. The scanning rates were set to 0.2  $\text{mV}/\text{s}$ . In a buffer solution with varying pH levels, the potential of yield ferrite (operating electrode) was determined against  $\text{Ag}/\text{AgCl}$  (reference electrode).

The Co-Fe alloy film was electrodeposited in an electrolyte bath, including (0.05 M  $\text{CoSO}_4 \cdot 7\text{H}_2\text{O}$  and 0.1 M  $\text{Fe}(\text{NH}_4)_2(\text{SO}_4)_2 \cdot 6\text{H}_2\text{O}$ ) alcoholic solutions. Galvanostatic operation was used to conduct the electrodepositioning experiments, and a constant current source of up to 1000 mA was used. The potentials were

all analysed in relation to (Ag/AgCl/sat KCl). By analysing electrochemically polarisation curves, metal and alloy deposited potentials were obtained. The ability to observe the deposit layer (uniformity) was also assessed. The layers were rinsed with dual-distilled water after formation and stored in a dissector. The alloy films were anodized at ambient temperature (25 °C). The CoFe<sub>2</sub> alloy layers serve as an anode, and the platinum serves as a cathode. At ambient temperature, an electrolyte of 1 M KOH aqueous solution was employed to crosslink oxygen species into CoFe<sub>2</sub> alloy sheets to create CoFe<sub>2</sub>O<sub>4</sub>.

Electrochemical reactions were carried out in a constant current. For 300 seconds, the alloy films were anodized to the matching hydroxides at a density of anodic current of 10 mA cm<sup>-2</sup>. The electroplating conditions (current density and time) were adjusted to keep the films attached to the substrates for a long-time following electrodeposition. Maintain anodization time and make current density optimisation [24].

Intercalation time was optimised once the current density was enhanced. After surface modification, the layers were rinsed with dual-distilled water and further characterised. The duration and anodization current density were changed to achieve good-adhered oxide layers on the anodes. The electrodeposition production factors were experimented at the ambient temperature (25 °C) [24].

Many defects, such as holes and voids, can be seen in freshly deposited films. Annealing the film in air or vacuum minimises flaws and improves particle size. The anodized alloy sheets underwent air annealing at various temperatures and times to improve the ferrite film's properties. The sheets were air-annealed at 400, 600, 700, and 800 °C for 2 hrs and were cooled to room temperature gradually in a furnace.

### 3. Results and discussion

#### 3.1 Preparation of CoFe<sub>2</sub>O<sub>4</sub> thin films by electrodeposition from non-aqueous media

##### 3.1.1 Cyclic voltammetry (CV) studies

In order to understand the electrochemical behaviour of the electrodeposition of CoFe<sub>2</sub> alloy, the cyclic voltammogram of each of the reacting components was studied alone and in admixture using a sulphate – ethanol bath.

##### 3.1.1.1. Cyclic voltammetry of cobalt sulphate (CoSO<sub>4</sub>)

As seen in Fig. 2a, cyclic voltammograms (CV) of 0.05 M CoSO<sub>4</sub> in ethanol at a scan rate of 10 mV/s without agitation. Voltametric analyses were performed in the potential range of 0 to -4 V with three different cathode electrodes: Pt, SS, and Cu. Each CV is distinguished by three cathodic peaks (C<sub>1</sub>, C<sub>2</sub>, C<sub>3</sub>) which appear at potentials equal to -1.82, -1.86, -2.44 V respectively, and one anodic peak (A<sub>1</sub>). Peaks C<sub>1</sub> and C<sub>2</sub> (E = -1.82, -1.86 V) describing the cobalt electrodeposition into the unblocked effective areas of the Pt and SS cathode surfaces [25]. The C<sub>3</sub> peak appeared at potential -2.44 V was ascribed to the electrodeposition of cobalt onto the energised active centres when desorbed molecules of ethanol were removed from the surface of the copper electrode [25].

Additionally, the large-scale deposition of Co also interjected to C<sub>3</sub>. On altering the scan to the positive direction, anodic peaks (A<sub>1</sub>) appeared at a voltage of -0.7 V, which were connected to the reoxidation of metallic cobalt created during the negative direction scan [25]

##### 3.1.1.2. Cyclic voltammetry of Fe (NH<sub>4</sub>)<sub>2</sub> (SO<sub>4</sub>)<sub>2</sub>

The nonlinear voltammogram of 0.1 M of ammonium ferrous sulphate in ethanol is illustrated in Fig. 2b. Two cathodic peaks were noticed on a Cu substrate with potentials of -1.8 and -2.8 V. Also, cathodic peaks were recorded at potential of -2.35 and -3.1 V on SS substrate. On the other hand, For the Pt substrate, one cathodic peak was found with a potential of -3 V with a non-stirred solution. Sulphate ions, which are involved in the electron transfer at low potential, have an impact on the cathode reaction rates and mass transfer coefficient [26-27].

These peaks have been attributed to ferrous ion reduction to metallic iron. when the scan direction was changed to positive, A single anodic peak was visible at -0.1 V in potential. This peak corresponds to the electro- termination of deposited iron. The iron layer thickness has been reported to be mass transfer dependent [28].

##### 3.1.1.3 Cyclic voltammetry of cobalt - iron alloy (CoFe<sub>2</sub>)

On specific substrates, cyclic voltammetry (CV), cathodic current density-time, and galvanostatic technique tests were carried out; Pt, SS, Cu are illustrated in Fig. 2c. Various substrates have different deposition potentials calculated from polarization curves. This variation could be attributed to anisotropic substrates and varied plane alignments from the substrate to the substrate. (As evidenced by the XRD

study). As a result, the degree of mismatching between the prepared particles and the platform produces diverse results from polarization curves. All CV studies began with a negative sweep from 0.0 V to -4 V a scan range of 10 mV s<sup>-1</sup>. Figure 2c illustrates the voltametric current fluctuation with potential for cobalt-iron alloy deposited on various cathodes at 10 mV s<sup>-1</sup> scan rate. Volumetric currents are found to be increased depending on the type of substrate surface, which may be due to the differences in the potential of each surface of the substrate. The value of the cathodic peak for CoFe<sub>2</sub> alloy on a Pt substrate appeared at a potential of -2.95 V. The deposited peak for CoFe<sub>2</sub> alloy on SS has been noticed at -2.42 and -2.74 V. But the deposited peak for CoFe<sub>2</sub> alloy on Cu has been noticed at -2, -2.6 and -3.1 V. As with dissolution, peaks are depicted at the potential -0.3 V for all alloy substrates.

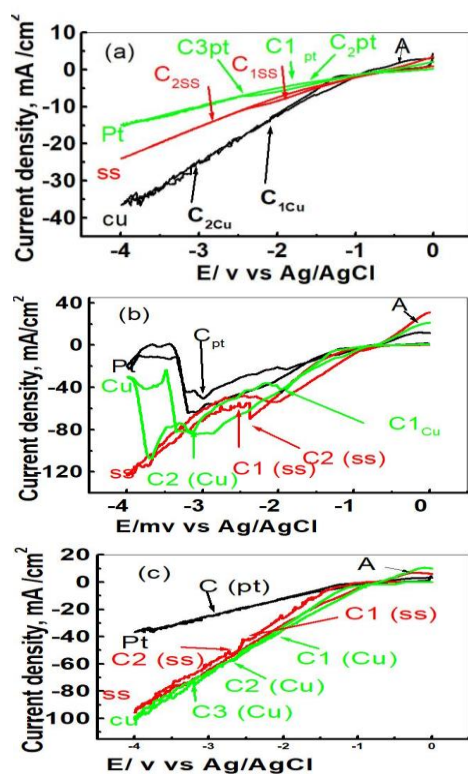


**Fig.2** Voltammograms obtained on different substrates in non-aqueous solution of a) 0.05 M CoSO<sub>4</sub>; b) 0.1 M Fe (NH<sub>4</sub>)<sub>2</sub> (SO<sub>4</sub>)<sub>2</sub>, c- CoFe<sub>2</sub> alloy, and solution of CoFe<sub>2</sub> alloy at SR (10 mV/s) and 0 rpm.

### 3.1.2. Linear Sweep Voltammetry (LSV)

This research sought to determine the current density variation in electroplating experiments as well as the impacts of mechanical stirring and bath temperatures on the cathodic performance of the electrolyte on different substrates.

#### 3.1.2.1. Effect of agitation for cobalt –iron alloy (CoFe<sub>2</sub>)

Bath stirring's effect on the deposition of CoFe<sub>2</sub> was examined using Pt, SS, and Cu substrates. For the CoFe<sub>2</sub> alloy on a Pt substrate, Figure 3a depicts three cathodic and three anodic peaks. primary cathodic peak (C<sub>1</sub>) was observed at a voltage of -2.950 V for a unstirred solution. This peak was caused by the co-deposition of the CoFe<sub>2</sub> alloy. When the solution is agitated at 200 rpm, the capacitance of cathodic peak's (C<sub>1</sub>) potential was moved to the peak (C<sub>2</sub>) at a voltage of -3.023 V. Furthermore, the applied current has shifted from -120 to -160 mA cm<sup>-2</sup>. Secondly, when the solution is agitated at 200 to 400 rpm, The density of current was changed from -160 to -200 mA/cm<sup>2</sup>, and the cathodic peak (C<sub>2</sub>) was moved to a peak (C<sub>3</sub>) at a potential of -3.200 V. Finally, (C<sub>4</sub>) appeared at a potential of -3.400 V when the agitation of the bath increased to 600 rpm.

At the same time, cobalt-iron alloy deposited on SS substrate from non-aqueous bath has been depicted in Fig 3.b. Figure 3b reveals that increasing stirring has accompanied an increment in the deposition potential and current density. When the rpm was raised from 0 to 200, the cathodic peak shifted from -2.3 V to -2.6. Further increasing of the stirring from 200 to 400 rpm, moved the applied current density from -47.8 to -78.13 mA cm<sup>-2</sup>, and at a potential of -2.70 V, the cathodic peak (C<sub>2</sub>) was displaced to peak (C<sub>3</sub>). When the bath was stirred from 400 rpm to 600 rpm, the fourth cathodic potential eventually developed at -2.855 V.

The CoFe<sub>2</sub> alloy deposited on the Cu substrate from an alcoholic bath has been described in Fig.3c. Figure 3c shows that rising agitation from 0 to 600 rpm is associated with an increasing deposition potential from -2.6 to -3.6 V respectively [29].

Agitation of the plating solution, in general, refills metal salts or particles at the cathode and lowers the width of the dispersal layer. It reduces the formation of gas bubbles, which could otherwise result in pits. Agitation can be increasing the operational current density and so allowing for a higher operating current density.

These parameters affect the morphology of the deposited alloy in addition to the concentration of metals, which responds for the loss of metal ions by discharge at the cathode more quickly. Because it ensures enough mixing of the metal salt for the deposition solution, an agitation system can considerably increase electrodeposition performance. This is true, however, if the other factors in the solution are correctly regulated [30]. A non-homogeneous layer

was always produced during deposition as a result of dehydrogenation shown to be more than expected. It has been discovered that the possibility for deposition of the  $MFe_2$  alloy is lower than that of M and larger than that of iron metal. This could be owing to the more noble metal is being a part of an alloy with other metal elements with a considerably lower voltage than that meta, deposition occurs at a lower potential [31].

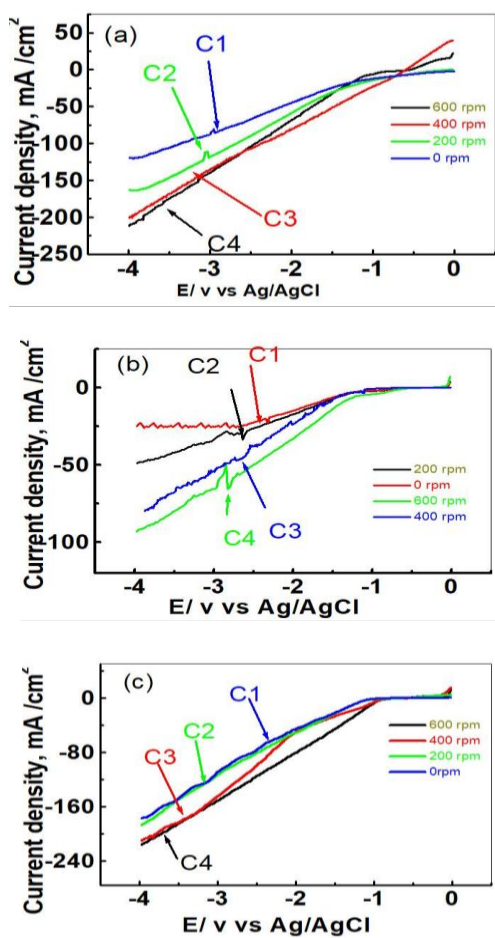


**Fig. 3** LSV curves obtained on a) Pt electrodes, b) on SS electrodes and c) on Cu electrodes in non- aqueous solution of  $CoFe_2$  alloy, scan rate ( $10\text{ mVs}^{-1}$ ) at different speed of stirring.

### 3.1.2.2. Effect of temperature for electrodeposition of $CoFe_2$ alloy

The influence of bath temperature on the decomposition potential of  $CoFe_2$  has been studied for the Pt substrate. The temperature of the bath ranged from 30 to 70 °C. Figure 4a depicts LSV curves for electrochemical deposition of  $CoFe_2$  alloy on Pt cathode from non-aqueous sulphate bath. The cathodic current grows quickly after potential application due to

crystallization begins and the reactive surface area of each crystal grows three-dimensionally quickly

An electro crystallization growth process in three dimensions [32]. It is observed that shifting the operating temperature from 30 to 50 °C led to a reduction in  $CoFe_2$  deposition potential from -2.950 V (peak C<sub>1</sub>) to -2.62 V (peak C<sub>2</sub>). In addition, growing the bath temperature from 40 to 60 °C resulted in a more positive shift in  $CoFe_2$  deposition potential from -2.62 V (peak C<sub>2</sub>) to -2.50 V (peak C<sub>3</sub>).

Also, Fig 4.b displayed a cobalt-iron alloy deposited on the SS substrate. Increasing the bath temperature leads to variations in the current density and deposition potential. Raising the bath temperature from 30 to 50 °C shifted the deposition potential from -2.5 to -2.19 V and the density of cathodic current varied from to -122 mA to -127 mA. The potential for a deposit was reduced from 2.19 V to -2 V and the current density was raised to -140 mA cm<sup>-2</sup> by raising the bath temperature further from 50 to 70 °C.

Finally, Fig. 4 focused on the changes in deposition potential values as a function of bath temperature value for the  $CoFe_2$  alloy co-deposited on the Cu substrate. Whereas the bath temperature increased, the current density increased and the plating potential decreased, i.e. at 70 °C, the value of the deposition potential was -2.29 V compared with -2.95 V at 30 °C.

The crystal size typically decreases as bath temperature rises and the polarisation values to drop. Additionally, increasing the bath temperature increases the ionic mobility and diffusion rate, which improves the deposition bath's conductivity. The deposit alloy including more noble metals may be the cause of the reduction in deposition potential as temperature rises [33]. Increasing the bath temperature improves solubility and, as a result, the transport number, which enhances the solution's conductivity. It also decreases the solution's viscosity, allowing the double layer to be replenished more quickly. The high bath temperature lowers the adsorption of hydrogen on the deposits, reducing stress and the risk of cracking [34].

### 3.1.3. Chronopotentiometric studies

Figure 5 a- c displays the chrono -potentiometric curves recorded during electrodepositing of cobalt-iron alloy on Pt, SS, and Cu substrates from a non-aqueous medium. Experiments were performed at room temperature without stirring.

#### 3.1.3.1. Suitable current density for deposition process

The galvanostatic curves for electrodepositing thin layers of the alloy  $\text{CoFe}_2$  from an alcoholic solution of  $0.05 \text{ M CoSO}_4 + 0.1 \text{ M Fe}(\text{NH}_4)_2(\text{SO}_4)_2$  are shown in Fig. 5. Formations were made at the current densities of  $-10, -20, -25, -28, -35, -40, -50, -60,$  and  $-70 \text{ mA cm}^{-2}$ , respectively. The value of potential has also been observed to change over time. When deposits are made, the potential grew to ascertain amount before rapidly decreasing to an equilibrium value. The rapid decline in potential indicated that the cathode surface was being covered quickly, whilst the steady state suggested that the cathode surface was practically finished. The values of deposition rate at current density of  $-35, -50$  and  $-50 \text{ mA cm}^{-2}$  were detected to be maximum with high film thickness on specific cathode. Thus, a current density of  $-35, -50, -50$  was considered suitable for the deposition of thin films on various cathode substrates respectively.

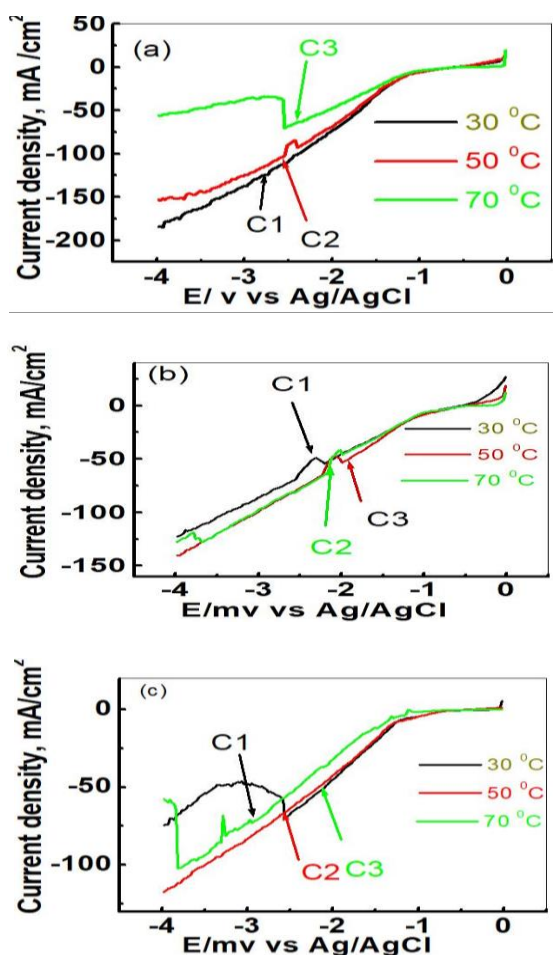


**Fig. 4** LSV curves obtained on a) Pt electrode, b) SS electrode and c) Cu electrode in non-aqueous solution of  $\text{CoFe}_2$  alloy, scan rate ( $10 \text{ mVs}^{-1}$ ), at different temperatures.

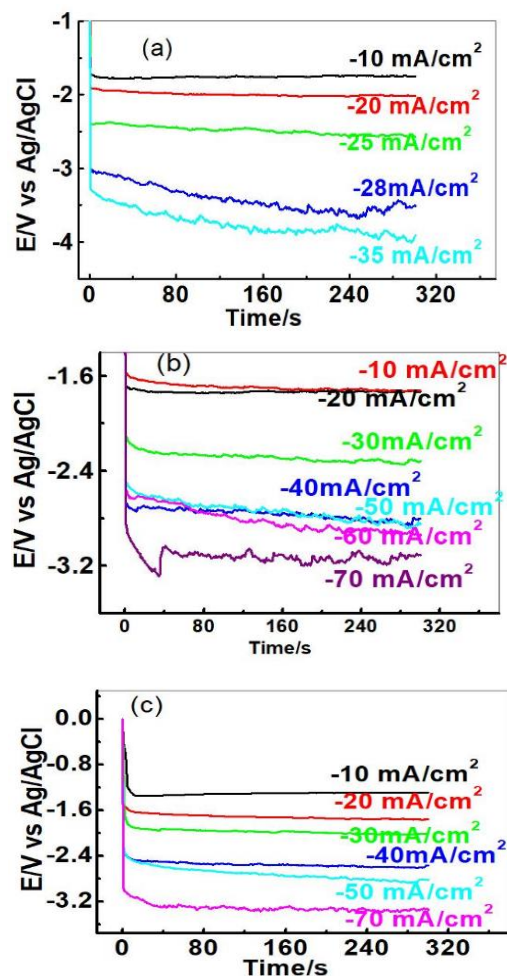


**Fig. 5** Variation of deposition potential with time at constant current density for  $\text{CoFe}_2$  on a) Pt, b) SS and c) Cu electrodes from alcoholic bath.

### 3.1.4. Influence of current density on $\text{CoFe}_2$ alloy current efficiency

For 300 seconds of deposition at room temperature, Fig 6 shows the relationship between current density and current efficiency on diverse cathodes (Pt, SS, and Cu). With increasing current density, the efficiencies rise, peak at the optimum current density, and then decrease as current density increases. Lower current efficiency occurs when metal deposition slows to the point where hydrogen evolution takes over as the primary process on the cathode [35]. Current efficiency improvements over the optimum current density simply enhance the rate of dehydrogenation by reducing the quantity of water molecules present [36].

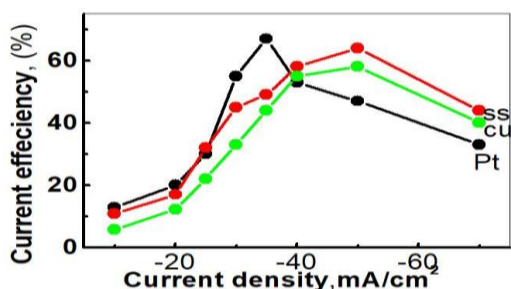


**Fig. 6** Variation of current efficiency with current density for a CoFe<sub>2</sub> alloy on Pt, SS, Cu substrates from non-aqueous bath.

Figure 6 shows that within the examined range, current efficiency is enhanced first by raising current density up to  $-50 \text{ mA cm}^{-2}$  and thereafter falls. Current efficiencies of 67%, 64%, and 58% have been achieved. For the alloys deposited on Pt, SS, and Cu substrate, at current densities of  $-35$ ,  $-50$ , and  $-50 \text{ mAcm}^{-2}$  respectively. With a further increase in the current density up to the optimum current density, The hydrogen reduction rate exceeds the rate of metal deposition. The growth in current density only resulted in an increase in the rate of hydrogen reduction, which decreased current efficiency.

### 3.1.5. Chronoamperometric studies

The electrocrystallization process of Fe, Co, and their alloys has been studied using chronoamperometry. It was allowed to identify the optimum potential range for enhancing potentiostatic deposition based on the voltammetric measurements.

Figure 7 displays the chronoamperometric curves recorded with Pt, SS and Cu cathodes in the deposition of CoFe<sub>2</sub> alloy from alcoholic non-aqueous solutions containing  $0.05 \text{ M CoSO}_4 + 0.1 \text{ M Fe}(\text{NH}_4)_2(\text{SO}_4)_2$ . In all cases, the bath temperature was  $25 \text{ }^\circ\text{C}$  and the agitation rate was  $0 \text{ rpm}$ .

#### 3.1.5.1. Suitable deposition potential of CoFe<sub>2</sub> alloy on substrates

The changing current with time at fixed potentials is shown in Fig. 7. Depositions at various potential values, such as  $-1.5$ ,  $-1.7$ ,  $-1.9$ ,  $-2$ ,  $-2.25$ ,  $-2.5$ ,  $-2.75$ , and  $-3 \text{ V}$ , were performed to determine the best potential for the deposition procedure. With Pt, SS, and Cu substrates, variations in current density were observed over time. At these fixed potentials, the deposition rate was found to be very high. The behaviour of the current changed in a similar manner during the early stages of deposition on platinum, but after 1 minute, the behaviour differed.

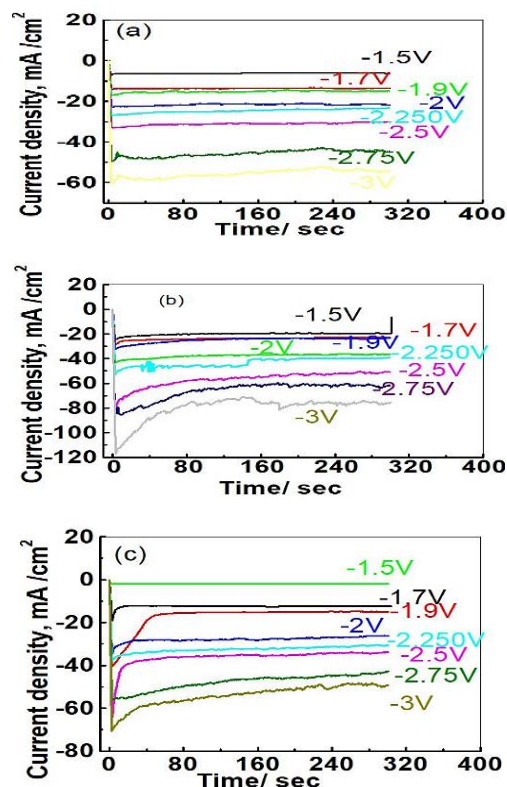


**Fig. 7** Variation of current density with time at constant potential for CoFe<sub>2</sub> alloy on a) Pt, b) SS and c) Cu substrates from alcoholic medium.

To begin, the current growth reaches a maximum in less than one minute and then rapidly decreases, reaching a steady state for all selected potentials. The rapid decrease in current reveals that the safety of the platinum surface was quickly completely covered by the CoFe<sub>2</sub> layer. At potentials of  $-1.5$ ,  $-1.7$ ,  $-1.9$ ,  $-2$ ,  $-2.25$ ,  $-2.5$ ,  $-2.75$ , and  $-3 \text{ V}$ , steady state current densities were  $-6.6912$ ,  $12.34$ ,  $-14.5$ ,  $-21.5$ ,  $-23.51$ ,  $-29.5$ ,  $-33.5$ , and  $-50 \text{ mAcm}^{-2}$ . at Pt, SS, and Cu, the maximum deposition rates corresponding to the highest film thickness were obtained at  $-2.75$ ,  $-2.5$ , and  $-3 \text{ V}$ , respectively. As a result, deposition potentials of  $-2.75$ ,  $-2.5$ , and  $-3 \text{ V}$  have been determined to be suitable [37].

### 3.1.6. The influence of current density on film thickness

Because most of a film's properties depend on its thickness, it is one of the most essential physical parameters. Numerous variables have been enhanced to achieve the terminal layer thickness, including concentration, film deposition time, and temperature. The method of measuring weight difference, which records the film's area and weight, was used to compute and record the film thickness [13,18,33]. The alloy

films are deposited for 300 seconds under optimal bath compositions at various applied currents. The variation of film thickness created on Pt, SS, and Cu with current density is shown in Fig. 8. For Pt, SS, and Cu substrates, almost linear correlations up to -35, -50, and -50 mA cm<sup>-2</sup> were reported, with corresponding film thicknesses of 4.9, 5.9, and 4.3 μm, respectively. When current density increases, a porous deposited film forms, the film's thickness decreases, and the film separates from the substrate as a result. [38].

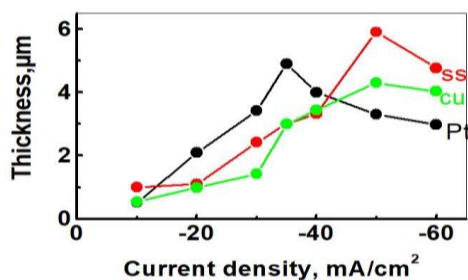


**Fig. 8** Variation of film thickness with current density for CoFe<sub>2</sub> alloy on (a- Pt, b- SS, c- Cu) electrodes from alcoholic medium.

### 3.1.7. Electrochemical performance of a CoFe<sub>2</sub>O<sub>4</sub> thin film

The corrosion examination of CoFe<sub>2</sub>O<sub>4</sub> thin layer on a variety of cathodes (Pt, SS, and Cu) in alcoholic sulfate bath shower started with checking the open circuit potential after drenching it into the testing solution for 300 seconds. This technique shows the oxidation propensity of a material in a corrosive environment. Out of all tested pH (1, 3, 7, 9, 12) the open circuit potential increased or decreased or is nearly consistent throughout time until it reached steady-state levels [39].

Cobalt's corrosion resistance in a complex solution is influenced by pH and the concentration of an oxidising agent. Cobalt seems to be completely corrodible in acidic solutions in the absence of oxidizers, and somewhat corrodible in alkaline or neutral solutions in the presence of oxidizers, and completely non-corrodible solutions that are neutral or slightly alkaline. In neutral or slightly alkaline solutions, an oxide layer will form and cover the surface [39]. From Fig. 9a the potential–time curves of the Pt substrate, the immersion potential ( $E_{im}$ ) has values ranging between -620 to -66 (mV). The steady state potential values ( $E_{ss}$ ) are almost the same as the ( $E_{im}$ ) values except at pH 7.0 where the ( $E_{ss}$ ) value is more

positive than the ( $E_{im}$ ) value of rusting control of the stainless steel substrate was increased by a thin film of oxides (chromium and iron oxides). The oxide layer is so dense that it successfully separates the steel from the environment while being only a few nanometers thick.

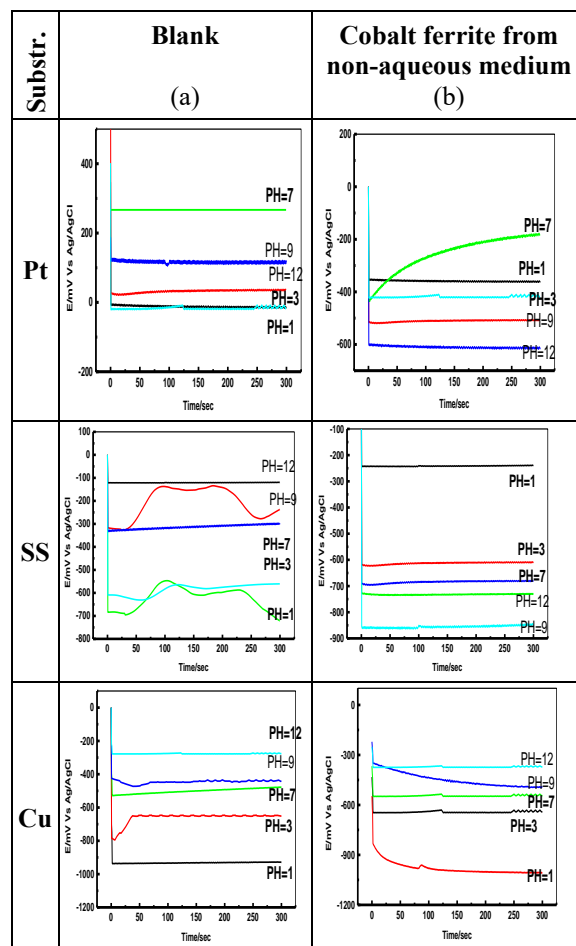


**Fig. 9** Potential-time curves of cobalt ferrite from (a) blank, (b) alcoholic medium on (Pt, SS, Cu) substrates in different pH solutions.

As an oxide layer builds on the metal, it becomes passivated, and the oxidation rate slows to less than 0.05 mm per year. Unfortunately, this perfect process does not always occur; without re-passivation, the oxide layer might be destroyed, resulting in significant corrosion. In Fig. 9b the values of ( $E_{im}$ ) are nearly identical to ( $E_{ss}$ ) at all pH settings, as can be seen from the SS results.

Figure 9b reveals that neutral solutions do not corrode the copper substrate but acid or alkaline solutions containing oxidization corrode it. Finally neutral or slightly alkaline solutions should passivate the metal in application. Furthermore, the pH values of 3, 7, and 12 are nearly identical to those of ( $E_{ss}$ ). All substrates exhibited the same behaviour at pH 1 and 9.

**3.1.8. Degree of oxide film thickening:**

Shams El-Din and Abd El-Kader (1979) [39] proposed an open circuit potential-based concept for film thickening on metal and alloy surfaces. The theory's basic principle is that Potential has been fixed by simultaneous anodic occurrences. (film formation) and cathodic (oxygen reduction) couplings, with the anodic reaction being rate limited. Straight lines were generated by offering the data as potential–log (time) curves, which satisfied the accompanying equation.

$$E = \text{constant} + 2.303(\delta / \beta) \log t \dots\dots\dots(1)$$

Where (E) was the electrode potential in relation to a saturated calomel electrode, (t) was the time from the moment of dipping in the solution, ( $\delta$ ) was the rate of oxide film thickening at each time,  $\beta$  was given by equation (2):

$$\beta = (nF / RT) \alpha \delta t \dots\dots\dots(2)$$

Where  $\alpha$  is the transfer coefficient related to that encountered in normal electrochemical reactions [20], ( $0 < \alpha < 1$ ), and  $\delta$  is the width of the initiation energy barrier to be traveled by the ion throughout oxide growth, R is the gas constant and T is the absolute temperature.

If the oxide layer on the substrate surface thickens as a result of the passage of  $Fe^{2+}$  ions to the oxide/metal boundary, then "n" in Eq. (2) becomes 2 and a becomes 0.5, 1 nm, and the consistency from Eq. (1) becomes 39.43 nm/V [40-44]. In Fig. (10), the slopes of the straight lines fixing the alteration of E with log t were used to compute the values of the oxide thickening rate.

When considering the physical properties of metal oxides that cover the cathode, this behaviour is easily understood. The following can be deduced from the curves of Fig. 10 and the values in Table 1:

a- The rate of  $CoFe_2O_4$  produced from alcoholic medium on SS, and Cu cathodes submitted advanced oxide film thickness at a pH range of 7 to 12, but on the Pt substrate it showed a decreased film thickness at the same pH range.

b- In the case of alkaline and acidic solutions, the film thickness was almost constant and independent of the solution's pH. The order of decrease in the rate of oxide layer thickening on Pt, SS, and Cu substrates from non-aqueous media can be followed by the electrodes in the current investigation

c- In neutral buffer solutions from alcoholic mediums, the rate of film thickness follows the order: Pt > Cu > SS.

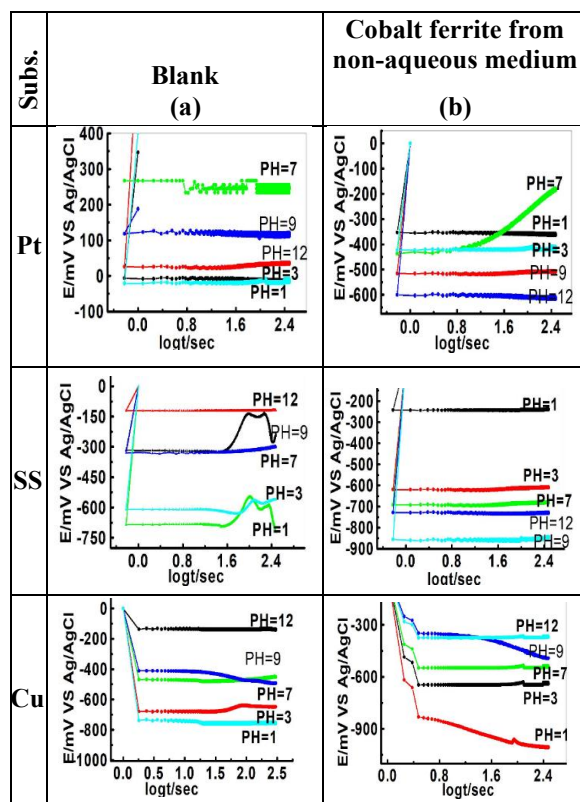


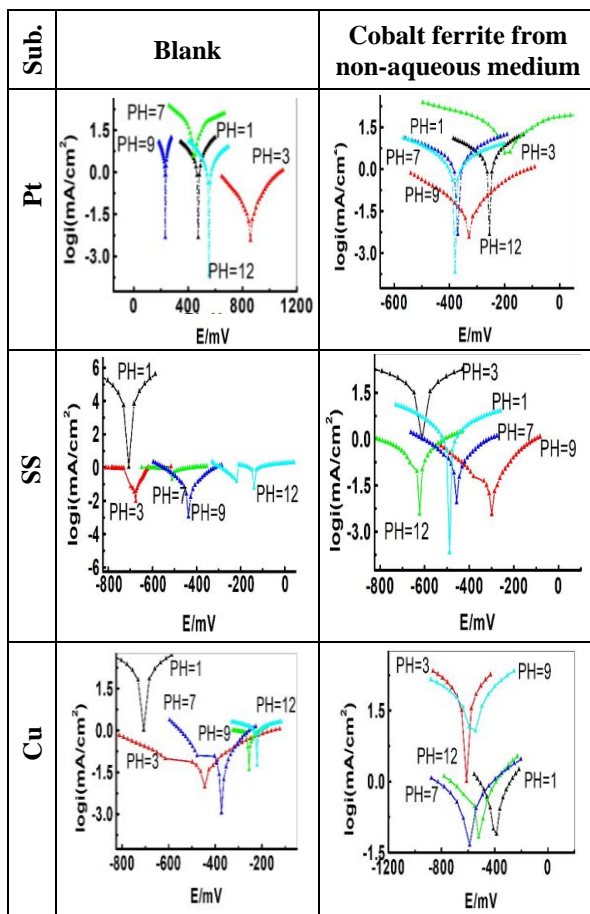
**Fig. 10** Potential-log t curves for cobalt ferrite from a- blank, b- non-aqueous medium) on (Pt, SS, Cu) substrates) in different pH solutions.

**Table 1** Values of E<sub>im</sub> and E<sub>s,s</sub> (mV) for cobalt ferrite in (Pt, SS, Cu) substrates.

Subs. pH	Pt		SS		Cu	
	E <sub>initial</sub> mV	E <sub>s,s</sub> Mv	E <sub>initial</sub> mV	E <sub>s,s</sub> mv	E <sub>initial</sub> mV	E <sub>s,s</sub> mv
1	-345	-365	-247	-243	-840	-1005
3	-418	-414	-613	-605	-648	-640
7	-423	-186	-686	-678	-536	-543
9	-514	-501	-861	-857	-338	-470
12	-597	-610	-731	-735	-357	-371

**3.1.9. Polarization measurements**

Figure 11 depicts Tafel plots polarization curves of dissimilar  $CoFe_2O_4$  thin film on different cathode surfaces of (Pt, SS, and Cu) in the buffer solution of different pH values in alcoholic sulfate bath. The corrosion kinetic parameters are listed in Table 2.



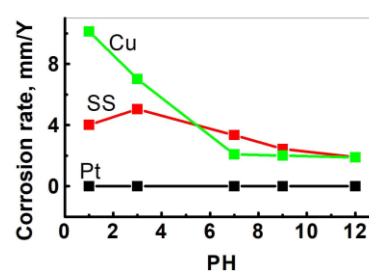
**Fig. 11** Tafel plots polarization curves for cobalt ferrite from for a) aqueous medium, b) alcoholic medium) on (Pt, SS, Cu) substrates in different pH solutions.

Table 2 Corrosion kinetic parameters.

Subst.	pH	RP $\square$	Ba $\square$	Be $\square$	-E $\square$	I $\square$	C.R $\square$	IE $\square$	Coeff.
		( $\Omega$ ) $\square$	mV/ $\square$	mV/ $\square$	m $\square$	mA/ $\square$	mpy $\square$	% $\square$	
			dec. $\square$	dec. $\square$	V $\square$	Cm $\square$			
Pt	1	24	183	-361	255	1.23	8.6	87	0.9
	3	154.86	242.8	-111.9	333.16	0.581	3.803	72.86	0.9994
	7	304.25	456.3	-853	113.08	1.40	9.08	99.01	0.9860
	9	55.88	66.13	-128.4	90.62	0.9823	7.491	85.58	0.8994
	12	612.03	252.4	-394.5	308.12	0.695	5.0043	78.22	0.9955
SS	1	575.7	131.4	-594	301.02	0.537	7.16	71.93	0.9987
	3	82.28	186.8	-102.7	408.21	0.582	7.211	71.67	0.9990
	7	679.45	222.3	-306	459.44	0.228	5.496	79.17	0.9244
	9	800.11	312.1	-512	624.6	0.207	4.33	76.17	0.9977
	12	896.43	360.3	-596	495.21	0.790	8.56	96.26	0.9999
Cu	1	23	223	-277	388	0.83	3.5	6.1	0.8
	3	156.01	131.4	-594	385.8	1.423	10.48	52.18	0.9249
	7	122.4	194	-585	275.02	1.7007	12.55	83.37	0.9099
	9	228.46	222	-293.7	389.44	1.0363	4.212	52.45	0.9888
	12	175.50	230.8	-212.5	293.20	0.9792	3.865	50.92	0.9830

The results revealed that resistance polarization (Rp), Tafel slopes ( $\beta_a$ ,  $\beta_c$ ), corrosion potential ( $E_{corr}$ ), corrosion current density ( $I_{corr}$ ) and corrosion rate (C.R.), are functions of pH values. The results showed

that; in acidic buffer solutions at pH equal to 1, 3, 7, cobalt ferrite deposited on Pt, SS, and Cu substrates were in active case and characterized by high corrosion current density. When the pH moved from acidic to neutral,  $I_{corr}$  values sharply increased by  $\approx$  74.6%, 93.73% and 92.3 % for Cobalt ferrites on Pt, SS and Cu substrates respectively. In the reverse direction, in alkaline buffer solutions with pH 9 and 12, the metal ferrites showed inactive behaviour, characterised by a reduced rate of corrosion. However, at highly alkaline pH 12, more safely layer may occur in the alcoholic medium. Ferrous oxide (FeO), on the contrary, is soluble at the pH above. As a result, more than accumulating on the metal surface to create a film, the oxide dissolves as it forms. The corrosion response is quicker than it is in acid solutions with a pH below 3 when the protective oxide coating is missing and the metal surface comes into direct contact with the acid solution. This means that the rate of corrosion is no longer solely determined by oxygen depolarization, but rather by a mixture of the two variables, namely hydrogen evolution and depolarization. [38-41]. Furthermore, metal ferrites exhibited two separate behaviours when the pH of the buffer was adjusted to neutral and alkaline solutions (pH = 7, 9, and 12 ). A stable passive state was reported in Co-ferrite, which could be attributable to the production of mixed oxide layers. The stable passive state of Co-ferrite from an alcoholic sulphate bath could only be generated in an alkaline solution. However, moderate and extremely acidic solutions have shown a large increase.



**Fig. 12** Corrosion rate versus pH curve for cobalt ferrite from non-aqueous medium) on (Pt, SS, Cu) substrates in different pH solutions.

The link between corrosion rate and pH is depicted in Fig.12. We may indicate that  $CoFe_2O_4$  thin film formed on Pt and Cu substrates from non-aqueous methane is used in the above studies.

### 3.2. Structural Characterization of $CoFe_2O_4$ .

As shown in Fig.13 a-c , the crystal structure of the spinel cobalt ferrite films produced on Pt, SS, and Cu

substrates with cathodic current densities of 35 mA cm<sup>-2</sup>, 50 mA cm<sup>-2</sup>, and 50 mA cm<sup>-2</sup>, respectively, is affected by annealing temperatures (400, 600, 700, 800 °C) for 2 hours. With the spinel ferrite phase and an annealing temperature of 600 °C, it is evident that hematite Fe<sub>2</sub>O<sub>3</sub> will form as a secondary phase on the Pt substrate. By raising the annealing temperature to 800 °C, CoFe<sub>2</sub>O<sub>4</sub> was converted into a single phase. The diffraction peak was found at 18.28°, 30.07°, 35.42°, 37.05°, 43.09°, 53.44°, 56.94°, 62.56°, and 74.01°, which match the diffraction planes (111), (220), (311), (222), (400), (422), (511), (440), and (533). These peaks revealed that extremely crystalline cubic spinel cobalt ferrite was produced. The most strong diffraction plane determines the crystallite size (311). When the Debye-Scherrer equation was used to analyse the different ferrite compositions that were created, it became clear that decreasing the crystallite size at an annealing temperature of up to 800 °C. XRD patterns for the SS substrate, Alternatively, revealed that an additional hematite phase was produced with ferrite phase of spinel at various annealing temperatures, varying from 400 °C to 800 °C for 2 hours, Fig. 13.b. Because ethanol served as a reducing agent, it produced iron oxide and cobalt metal particles, which is how this hematite phase came to be [28].

The presence of tiny grains is attributable to the low peak intensities in the XRD pattern. The Debye-Scherer equation revealed that the crystallite size dropped with the annealing temperature, from 164.6 nm at 400 °C to 114 nm at 800 °C. The plane (533) appeared on the Pt substrate. On the Pt substrate, the plane (533) appeared. Fig.13. c reveals the XRD patterns of CoFe<sub>2</sub>O<sub>4</sub> deposited on Cu substrate using alcoholic bath and then annealed at various temperatures between 400 and 800 °C.

At low annealing temperatures of 400 and 600 °C, hematite Fe<sub>2</sub>O<sub>3</sub> was identified as another phase of impurities. The development of a single phase of CoFe<sub>2</sub>O<sub>4</sub> was achieved by raising the annealing temperature to 800 °C. The produced film's crystallite size was reduced from 244 nm at 400°C to 137.5 nm at 800°C. The size of crystallites from the most intense peak of cobalt ferrites formed on Pt, SS, and Cu substrates was determined to be around 43, 77, and 102 nm, respectively, according to the Scherer equation.

The morphology of the electrode substrate, definite free surface energy, formation energy, electrode surface frame orientation, and crystallographic structure distortion at the nucleus-substrate interface boundary all have an impact on the nucleation on the electrode substrate, which could explain the variation

in the average size of crystallites with different crystallographic structures. Each cathode also has its own free surface energy and conductivity. The conductivity of each substrate is inversely proportional to its specific free surface energy. The conductivity of each substrate has an important effect on the rate of deposition reaction and crystal size. The substrate has a thicker coating in general.

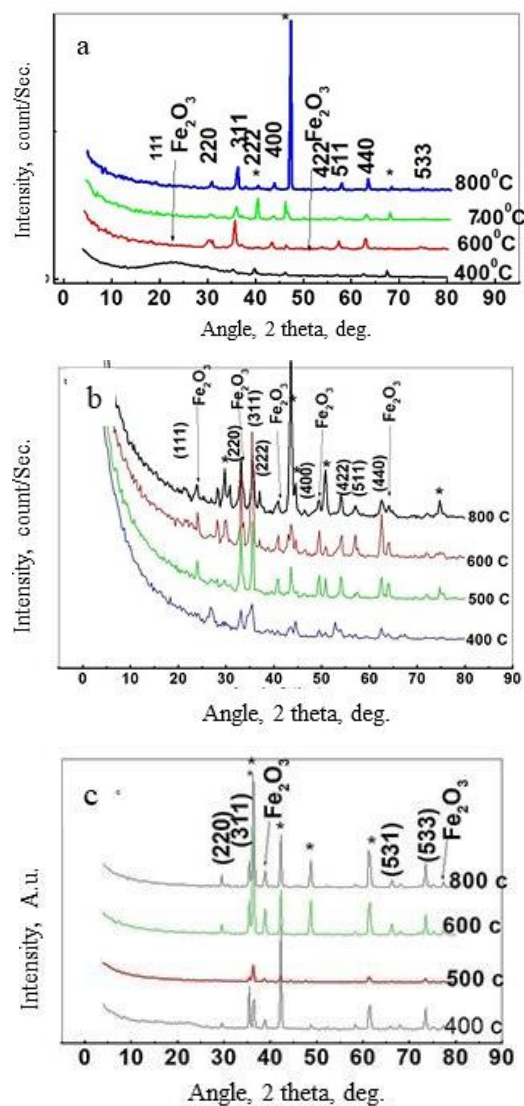


**Fig. 13** XRD patterns of CoFe<sub>2</sub>O<sub>4</sub> Ferrites electrodeposited from non-aqueous sulphate bath on a- Pt, b-SS, c- Cu substrates.

### 3.3. Magnetic properties of the CoFe<sub>2</sub>O<sub>4</sub> thin film

The hysteresis loop of electrodeposited cobalt ferrite at different temperatures for different substrates is shown in Fig 14 a-c (Pt, SS and Cu). Table 3 also has the information. The results demonstrated that raising the annealing temperature from 400 to 800 °C increased

the saturation magnetization, which was explained by increasing the crystallite size in addition to the homogenous and clear microstructure [29]. As compared to chemically synthesised  $\text{CoFe}_2\text{O}_4$  thin films,  $\text{CoFe}_2\text{O}_4$  thick films are in a quasi-free condition with little shear stress from the substrate. [30] All films on the Pt substrate obtained saturation below 48 emu/g, which is attributable to surface imperfections and shape. or pulse laser formed  $\text{CoFe}_2\text{O}_4$  epitaxial thin film [31]. The saturation magnetization has drastically increased due to a reduction in internal strain and defect density, principally as a result of greater temperature. Magnetic anisotropy, including magnetocrystalline and strain-induced anisotropies, has a significant impact on the coercive force  $H_c$ . The temperature at which the crystals were annealed reduced crystal flaws and internal stresses. The coercivity has fallen due to a decrease in magnetic anisotropy [32–40].  $\text{CoFe}_2\text{O}_4$  on SS from a non-aqueous liquid is shown in Fig. 14.b as plots of magnetization ( $M$ ) as a function of applied field ( $H$ ) at various annealing temperatures. The magnetic issues are listed in Table 2. At 800 °C for 2 hours, high saturation magnetic induction (43.3 emu/g) can be attained. This is a lower value than the bulk value (56emu/g). This is more than likely owing to an inert or dead layer at the nanoparticles' surface (shell) that inhibits the core ferromagnetic spins from aligning along the field direction. As a result, the saturation magnetization of nanoparticles has dramatically lowered. Another reason for the lower magnetism in nanoparticles is the canted spins or spin glass-like layer at the surface of the nanoparticles, It happens because the surface-to-volume atom ratio is larger for small particles.

With regard to these nanoparticles' saturation magnetization is reduced by the canted spins. Even at very high temperatures, no complete saturation in nanoparticles is attained due to this phenomenon (canted spins) at the surface (shell). This could be because  $\text{Fe}_2\text{O}_3$  is present. The results showed that as the saturation magnetization rose, the annealing temperature went up to 800 °C, explaining the basis for the growth in crystallite size, homogeneous and clear microstructure. Coercive power is the influence of magnetic anisotropy on  $H_c$ , including magnetocrystalline and strain-induced anisotropies, which is substantial. Crystal imperfections and internal stresses were reduced as the annealing temperature was raised. Consequently, the shrinkage of magnetic anisotropy and growth of crystallite size, the coercivity was reduced [36-37]. Figure 14.C shows variations in saturation magnetization, coercivity, and remanence

magnetization for  $\text{CoFe}_2\text{O}_4$  on Cu substrate from an alcoholic bath annealed at various temperatures. Table 3 also contained the appropriate magnetic parameters.  $\text{CoFe}_2\text{O}_4$  nanoparticles have a measured saturation magnetization ( $M_s$ ) value of 41.4 emu/g, which is less than the bulk's stated value of 55 emu/g. The decrease in the density of magnetization of nanoparticles in contrast to the bulk is caused by surface defects and shape.

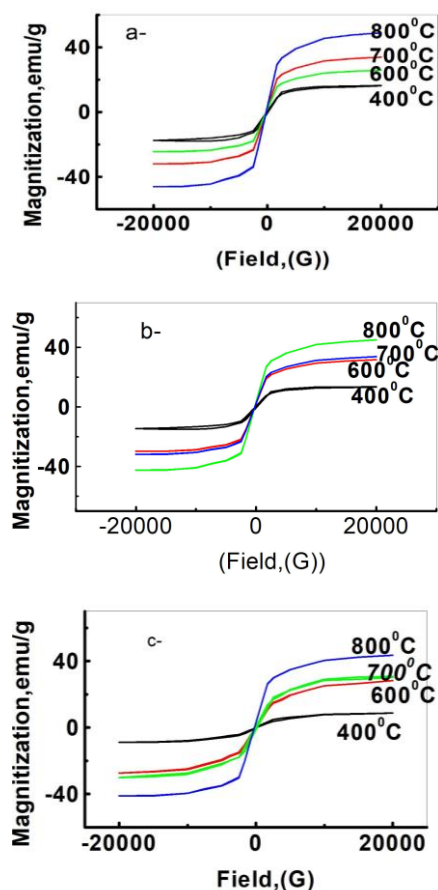


**Fig. 14** Effect of annealing temperature on M-H hysteresis loop of  $\text{CoFe}_2\text{O}_4$  annealed at 400, 600, 700 and 800 °C.

The finite-size scaling of nanocrystallites results in surface imperfections, which indicates to non-collinearity of magnetic moments on their surfaces.  $M_s$  and  $M_r$  values were improved by rising the temperature from 400 to 800 °C, which was caused by spin non-collinearity at the crystal surface. The samples' varying magnetic characteristics result from variations in crystallinity and crystallite sizes as a function of calcination temperature.

The number of molecules in a single magnetic domain is proportional to the energy of a magnetic particle in the external field. As a result, the reduction

in Ms with decreasing particle sizes can be attributed to surface effects caused by nanocrystallites scaling to finite sizes [38-45]. Saturation magnetization improves as the temperature rises, owing to the shrinking of the inter- and intragranular pores caused by higher firing temperatures. The presence of such pores creates a discontinuity that prevents the domain walls from moving. The temperature has a very minor effect on remnant magnetic induction. On the other hand, as the temperature rises, the coercive force drops dramatically [46]. The existence of the hematite impurity  $\text{Fe}_2\text{O}_3$  phase with the generated cobalt ferrite is responsible for the strong coercive force. A lack of long-range atomic order, related to that of liquid staining, is typically seen in nanocrystalline thin films.

Table 3 Effect of annealing temperature on magnetic properties of  $\text{CoFe}_2\text{O}_4$  thin films on different substrates (Pt, SS, Cu) from alcoholic medium.

Subs.	Temp. °C	Cryst. size (nm)	Magnetic properties			
			$M_s$ emu/g	$M_r$ emu/g	$H_c$ G	$M_r/M_s$
Pt	400	42	16.1	4.61	300	0.2
	600	55	25.8	8.61	222	0.3
	700	87	33.8	11.2	118	0.3
	800	107	48.7	16.4	103	0.3
S.S	400	77	13.4	3.8	566	0.2
	600	95	31.6	10.5	402	0.3
	700	104	33.4	11.1	306	0.3
	800	114	43.3	14.9	210	0.3
Cu	400	90	8.2	1.21	1102	0.1
	600	102	22	5.55	976	0.2
	700	124	30.8	7.07	754	0.2
	800	137	41.4	14.4	543	0.3

### 3.4. Morphological Characterization

In a non-aqueous media, Fig. 15 displays the surface morphology of cobalt ferrite on Pt, SS, and Cu substrates. The specimens were examined under a microscope with a magnification of 10,000. The micrograph of a cobalt ferrite surface on a Pt substrate (Fig. 15.a) exhibits a dendritic (tree-like) structure with regular forms and particles and chains typically less than 142 nm. The crystals' edges are a little wonky. On the other hand, SEM of Co ferrite on SS showed distorted needle structure and leaf-like morphology having a typical particle size of 154 nm, Fig. 15.b. SEM micrographs of ferrite film on Cu, on the other hand,

show a disordered agglomeration structure with a narrow particle distribution (Fig.15c).

The microstructure of the films on Pt substrate at different pH values has strongly affected by the pH changes. At low pH values (1,3), the SEM micrographs appear as agglomerated arboreal grains with a high grain size. Increasing the pH value from 7 to 12 as represented in Fig. 16 showed a flowery like structure with a low grain size of the crystals. Fig. 16 shows the SEM micrographs of films deposited on the SS substrate. Micrographs of ferrite films at blank pH show vertical triangle grains growing vertically on the SS substrate. At a low pH value (1), the SEM micrographs appear as cracked islands dispersed on the surface. When the pH is raised above 7, the SEM micrographs become spongier, with a high structure and a low cracked-like structure.

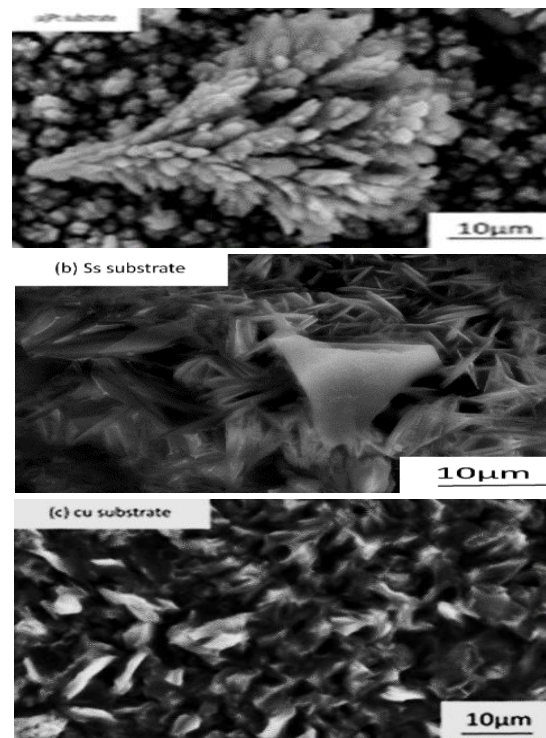
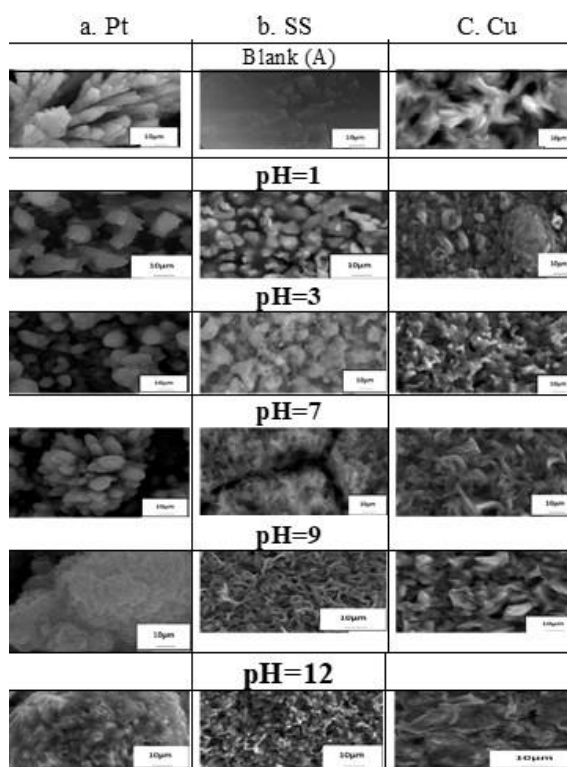


Fig. 15 SEM images of  $\text{CoFe}_2\text{O}_4$  Ferrites electrodeposited from non-aqueous sulphate bath on (a- Pt, b- SS and c- Cu) substrates.



**Fig. 16.** SEM images of cobalt Ferrite on ( a-Pt, b-SS, c- Cu) substrates from Non aqueous medium before and after exposure to different pH solutions.

#### 4. Conclusions

- The Nanocrystalline cobalt ferrite  $\text{CoFe}_2\text{O}_4$  thin film on different cathodes (Pt, SS, and Cu) has been synthesized via an electrodeposition– anodization process from an alcoholic medium.

- According to geotechnical studies, the optimal current density for synthesized film on (Pt, SS, Cu) substrates that satisfy the best properties is -35 and -50  $\text{mA}/\text{cm}^2$ , respectively, resulting in high current efficiency (67%, 64%, 58%) and film thickness (4.9 m, 5.9 m, 4.3 m).

- potentiostatic studies revealed that the best potential was for the preferred films on various substrates (-2.75 V, 2.5 V V), which fit well with the current densities and the accuracy of the results.

- When cobalt ferrite thin films are annealed at 800 °C, they have good conductivity and magnetic properties.  $M_s$  value 48.7 emu/g on Pt substrate with particle size 107 nm,  $M_s$  value 43.3 emu/g on SS substrate with particle size 114 nm and  $M_s$  value 41.4 emu/g on Cu substrate with particle size 137.5 nm.

- Synthesized cobalt ferrites on various substrates in alcoholic medium activate the surface of the films to

make them more hydrophilic, which led to their preferred use in medical and electrical applications, which is solubility.

- The corrosion investigation of  $\text{CoFe}_2\text{O}_4$  thin film on different substrates (Pt, SS, and Cu) in a non-aqueous sulfate bath began with monitoring the OCP. The order of decreasing the rate of oxide film thickening on (Pt, SS, and Cu substrates) can follow the following order: In neutral buffer solutions,  $\text{Pt} > \text{Cu} > \text{SS}$ .

- From the previous study, we can suggest that  $\text{CoFe}_2\text{O}_4$  thin film can be used safely in aqueous media in neutral and alkaline atmospheres for Pt, SS and Cu substrates, but it can not be used in acidic atmospheres for all substrates.

#### References

- [1] A. Manikandan, R. Sridhar, S.A. Arul and S.A.Ramakrishna, simple aloe vera plant-extracted microwave and conventional combustion synthesis: Morphological, optical, magnetic and catalytic properties of  $\text{CoFe}_2\text{O}_4$  nanostructures. *J Molec Struct.* 1076 (2014) 188–200.
- [2] P. Lorrain, F. Lorrain and S. Houle ,Magneto-Fluid Dynamics Fundamentals and Case Studies of Natural Phenomena Series: Astronomy and Astrophysics Library. Springer, Americas. (2006).
- [3] F. Li, H. Wang, L. Wang and J. Wang, Magnetic properties of  $\text{ZnFe}_2\text{O}_4$  nanoparticles produced by a low-temperature solid-state reaction method *Journal of Magnetism and Magnetic Materials.* 309 (2007) 295–299.
- [4] M.M. Rashad, E.M. Elsayed, M.M. Moharam, R.M. Abou-Shahba, AE..Saba, The structure and magnetic properties of  $\text{Ni}_x\text{Zn}_{1-x}\text{Fe}_2\text{O}_4$  nanoparticles prepared through Co-precipitation method.*J Alloys Compd.* 486 (2009) 759–767.
- [5] A .E . Saba , E. M. Elsayed, M. M. Moharam and M. M. Rashad, Electrochemical synthesis of nanocrystalline  $\text{Ni}_{0.5}\text{Zn}_{0.5}\text{Fe}_2\text{O}_4$  thin film from aqueous sulfate bath. *ISRN Nanotechnol.* 2012 (2012) 1–8.
- [6] E. M. Elsayed, M. M. Rashad, H. F. Y. KHalil, M. R. Hussien, M. M. B. EL-Sabbah and I. A. Ibrahim, The effect of solution pH on the electrochemical performance of nanocrystalline metal ferrites  $\text{MFe}_2\text{O}_4$  (M=Cu, Zn, and Ni) thin films. *Applied Nanoscience.* 6 (2016) 485-494.
- [7] E. M. Elsayed, M. M. Rashad, H. F. Y. KHalil, M. R. Hussien, M. M. B. EL-Sabbah and I. A. Ibrahim, Synthesis of Nanocrystalline Copper

- Ferrite film by Electrochemical Technique for Toxic Gas Sensing, Li Ion Batteries and Medical Applications. *Journal of Renewable Energy and Sustainable Development (RES D)*. 3 (2017) 2356-8569.
- [8] E. M. Elsayed, M. M. Rashad, M. M. Moharam, M. R. Hussien, M. M. B. EL-Sabbah and I. A. Ibrahim, electrodeposition-anodization preparation of nanocrystalline nickel ferrite films from aqueous sulfate solutions: a material for sensing of toxic household gases and health monitoring. *Journal of Intelligent System in Manufacturing (Intellkt.Sist.Proizv)*. 3 (2018) 169-178.
- [9] S.Y. Srinivasan, K. M. Paknikar, D. Bodas and V. Gajbhiye, Applications of cobalt ferrite nanoparticles in biomedical nanotechnology. *Nanomedicine (Lond.)* 13 (2018) 1221–1238
- [10] L. Ajroudi, N. Mliki, Bessais, L. V. Madigou, S. Villain and Ch. Leroux, Magnetic, electric and thermal properties of cobalt ferrite nanoparticles. *Materials Research Bulletin*. 59 (2014) 49-58
- [11] Y. M. Abbas, S. A. Mansour, M. H. Ibrahim and E. A. Shehab, Microstructure characterization and cation distribution of nanocrystalline cobalt ferrite. *Journal of Magnetism and Magnetic Materials*. 323 (2011) 2748–2756.
- [12] I. Sharifi, H. Shokrollahi, and S. Amiri, Ferrite-based magnetic nanofluids used in hyperthermia applications. *Journal of Magnetism and Magnetic Materials*. 324 (2012) 903–915.
- [13] C. D. Lokhande, S. S. Kulkarni, R. S. Mane and S-H. Han, Copper ferrite thin film: single-step non-aqueous growth and properties. *J. Cryst.Growth*. 303 (2007) 387–390.
- [14] M. Maxfield, H. Echaedt, Z. Equabla, F. Reidinger and R. H. Baughman, Bi-Sr-Ca-Cu-O and Pb-Bi-Sr-Ca-Cu-O superconductor films via an electrodeposition process. *Applied Physics Letters*. 54 (1989) 1932.
- [15] S. D. Sartale, C. D. Lokhande and M. Muller, Electrochemical synthesis of nanocrystalline CuFe<sub>2</sub>O<sub>4</sub> thin films from nonaqueous ethylene glycol medium. *Mater Chem Phys*. 80 (2003) 120–128.
- [16] C. R. Warren, Synthesis, Characterization, and Functionalization of Magnetic Iron Nanoparticles for Enhanced Biological Applications. PhD. thesis, Virginia Commonwealth University, USA, (2013).
- [17] Y. Konishi, T. Nomura, K. Mizoe and K. Nakata, Preparation of Cobalt Ferrite Nanoparticles by Hydrolysis of Cobalt-Iron (III) Carboxylate Dissolved in Organic Solvent. *Materials Transactions*. 45 (2004) 81 -85.
- [18] A. Takayama, M. Okuya and S. Kaneko, Spray pyrolysis deposition of NiZn ferrite thin films. *Solid State Ionics*. 172 (2004) 257-260.
- [19] S. M. Chavana, M. K. Babrekar, S. S. Moreb and K. M. Jadhav, Structural and optical properties of nanocrystalline Ni-Zn ferrite thin films. *Journal of Alloys and Compounds* 507 (2010) 21–25.
- [20] A. E. Saba, E. M. Elsayed, M. M. Moharam, M. M. Rashad and R. M. Abou-Shahba, Structure and magnetic properties of Ni<sub>x</sub>Zn<sub>1-x</sub>Fe<sub>2</sub>O<sub>4</sub> thin films prepared through electrodeposition method. *J. Mater. Sci*. 46 (2011) 3574–3582.
- [21] M. Maxfield, H. Echaedt, Z. Equabla, F. Reidinger and R.H. Baughman, Bi-Sr-Ca-Cu-O and Pb-Bi-Sr-Ca-Cu-O superconductor films via an electrodeposition process. *Applied Physics Letters*. 54 (1989) 1932.
- [22] S. D. Sartale, C. D. Lokhande and M. Muller, Electrochemical synthesis of nanocrystalline CuFe<sub>2</sub>O<sub>4</sub> thin films from nonaqueous ethylene glycol medium. *Mater Chem Phys*. 80 (2003) 120–128.
- [23] I. A. Rahman and V. Padavettan, Synthesis of Silica Nanoparticles by Sol-Gel: Size-Dependent Properties, Surface Modification, and Applications in Silica-Polymer Nanocomposites—A Review. *Journal of Nanomaterials*. 15 (2012) 2012 : doi:10.1155/2012/132424.
- [24] S. M. Chavana, M. K. Babrekar, S. S. Moreb and K. M. Jadhav, Structural and optical properties of nanocrystalline Ni-Zn ferrite thin films. *Journal of Alloys and Compounds*. 507 (2010) 21–25.
- [25] A. E. Saba, E. M. Elsayed, M. M. Moharam, M. M. Rashad and R. M. Abou-Shahba, Structure and magnetic properties of Ni<sub>x</sub>Zn<sub>1-x</sub>Fe<sub>2</sub>O<sub>4</sub> thin films prepared through electrodeposition method. *J. Mater. Sci*. 46 (2011) 3574–3582.
- [26] O. O. Ajibola, D. T. Olorunboba and B. O. Adewuyi, Effects of hard surface grinding and activation on electroless-nickel plating on cast aluminium alloy substrates. *Journal of Coatings*. 8 (2014) 334-344.
- [27] E. Gómez, S. Pané and E. Vallés, Magnetic composites CoNi–barium ferrite prepared by electrodeposition. *Electrochemistry Communications*. 7 (2005) 1225-1231.

- [28] M. M. Moharam, "Electrochemical preparation of nano-crystalline ferrites films suitable for electronic applications" MSc. Thesis, Al-Azhar University, Egypt (2011).
- [29] J. C. Ballesteros, P. Diaz-Arista, Y. Meas, R. Ortega, and G. Trejo, Zinc electrodeposition in the presence of polyethylene glycol 20000, *Electrochim. Acta.* 52 (2007) 3686-3696.
- [30] A. F. Gil, L. Salgado, L. Galicia and I. González, Predominance-zone diagrams of Fe (III) and Fe (II) sulfate complexes in acidic media. Voltammetric and spectrophotometric studies, *Talanta.* 42( 1995) 407–414.
- [31] A. F. Gil, L. Galicia, I. González, Diffusion coefficients and electrode kinetic parameters of different Fe(III) -sulfate complexes, *Journal of Electroanalytical Chemistry.* 417( 1996) 129–134.
- [32] F. J. Miranda, O. E. Barcia, S. L. Diaz, O. R. Mattos, and R. Wiart, Electrodeposition of Zn-Ni alloys in sulfate electrolytes, *Electrochim. Acta.* 41 (1996) 1041-1049.
- [33] R. Rashkov, S. Zsuzsa, B. Jóni, M. Arnaudova, I. Bakonyi, and L. Péterb, Compositional, Structural and Magnetic Study of Layered Co-Mn-O-B Deposits Formed during Potentiostatic Electrodeposition Exhibiting Current Oscillations, *Journal of The Electrochemical Society.* 164 (2017) 908-915
- [34] P. Milan and S. Mordechay, Toronto. A Wiley-Interscience Publication, John Wiley & Sons, Inc. (1998). 124-125.
- [35] A. Brenner, *Electrodeposition of alloys. Vol. I and II* (Academic Press, New York 1963).
- [36] E. M. Elsayed, A. E. Shalan, M. M. Rashad. Preparation of ZnO nanoparticles using electrodeposition and co-precipitation techniques for dye-sensitized solar cells applications, *Journal of Materials Science: Materials in Electronics.* 25 (2014) 3412-3419.
- [37] S. D. Sartale and C. D. Lokhande, Room temperature preparation of NiFe<sub>2</sub>O<sub>4</sub> thin films by electrochemical route, *Indian Journal of Engineering and Materials Science.* 7 (2000) 404-410.
- [38] S. Kumar, S. Pande and P. Verma, Factor Effecting Electro-Deposition Process, *International Journal of Current Engineering and Technology.* 5 (2015) 700-703.
- [39] N. Zech, E.J. Podlaha, and D. Landolt, *Journal of the Electrochemical Society.* 146 (1999) 2886
- [40] V. Narasimhamurthy and B.S. Sheshadri, Electrodeposition of Zinc-Cobalt Alloy from an Alkaline Sulfate Bath Containing Triethanolamine and Gelatin *Journal of Metal Finishing.* 96 (1998) 24-27.
- [41] T. Pauporte and D. Lincot, Electrodeposition of semiconductors for optoelectronic devices: results on zinc oxide, *Electrochimica Acta.* 45 (2000) 3345-3353.
- [42] E. M. Elsayed, M. M. Rashad, M. R. Hussien, M. M. B. EL-Sabbah and I. A. Ibrahim, Electrochemical synthesis of nanocrystalline NiFe<sub>2</sub>O<sub>4</sub> Thin film from aqueous sulphate bath, *Journal of alloys and compounds.* 798 (2019) 104-111.
- [43] E. M. Elsayed M. M. Rashad, H. F. Y. Khalil, I. A. Ibrahim, M. R. Hussein and M. M. B. El-Sabbah, The effect of solution pH on the electrochemical performance of nanocrystalline metal ferrites MFe<sub>2</sub>O<sub>4</sub> (M=Cu, Zn, and Ni) thin films" *Appl Nanosci.* 6 (2016) 485–494.
- [44] S. S. Arvapalli, B. Talluri, K. Anbalagan and T. Thomas, Role of pinning mechanism in co-precipitation derived cobalt rich, cobalt ferrite nanoparticles," *Condensed Matte.* (2017).
- [45] U. S. Sharma, R. N. Sharma and R. Shah Int. Physical and Magnetic Properties of Manganese Ferrite Nanoparticles, *Journal of Engineering Research and Applications, Physical and Magnetic Properties of Manganese Ferrite Nanoparticles.* 4 (2014) 14-17.
- [46] Z. Ai, W. Sun, J. Jiang, D. Song, H. Ma, J. Zhang and D. Wang, Passivation Characteristics of Alloy Corrosion-Resistant Steel Cr10Mo1 in Simulating Concrete Pore Solutions: Combination Effects of pH and Chloride, *Materials.* 9 (2016) 749.